KINETICS OF PROPYLENE EPOXIDATION OVER EXTRA-CRYSTALLINE GOLD ACTIVE SITES ON AU/TS-1 CATALYSTS

JEREMY W. ARVAY[1], WEI HONG[2], CHRISTINA LI[2], W. NICHOLAS DELGASS[1,†], FABIO H. RIBEIRO[1], JAMES W. HARRIS[3,*]

[1]CHARLES D. DAVIDSON SCHOOL OF CHEMICAL ENGINEERING, PURDUE UNIVERSITY, 480 STADIUM MALL DRIVE, WEST LAFAYETTE, IN 47907, USA.

[2]DEPARTMENT OF CHEMISTRY, PURDUE UNIVERSITY, 560 OVAL DRIVE, WEST LAFAYETTE, IN 47907, USA.

[3]DEPARTMENT OF CHEMICAL AND BIOLOGICAL ENGINEERING, THE UNIVERSITY OF ALABAMA, 3043 H. M. COMER HALL, 245 7TH AVENUE, TUSCALOOSA, AL 35487, USA.

*Corresponding author: james.harris@eng.ua.edu

KEYWORDS: Epoxidation, gold, propylene oxide, hydrogen peroxide, partial oxidation

ABSTRACT: To determine whether the catalytic roles of extracrystalline and intracrystalline gold nanoparticles supported on titanosilicate-1 (TS-1) for direct propylene epoxidation are intrinsically different, the kinetics of direct propylene epoxidation were measured in a gas-phase continuous stirred tank reactor (CSTR) over polyvinylpyrrolidone-coated (PVP) gold nanoparticles (Au-PVP/TS-1) deposited on TS-1. The as-made PVP-coated gold nanoparticles were too large to fit into the micropores of TS-1, even after ligands were removed *in situ* by a series of pretreatments, as confirmed by both TEM and TGA-DSC. The activation energy (51 kJ mol^{-1}) and reaction orders for H_2 (1.3), O_2 (0.4), propylene (0.4), propylene oxide (-0.6), carbon dioxide (0), and water (0) for propylene epoxidation measured on Au-PVP/TS-1 were consistent with those reported for Au/TS-1 prepared via deposition-precipitation (Au-DP/TS-1) (52 kJ mol^{-1}, H_2: 1, O_2: 0.4, C_3H_6: 0.4, C_3H_6O: -0.6, CO_2: 0, H_2O: 0). However, while the reaction orders for hydrogen oxidation on Au-PVP/TS-1 (H_2: 0.8, O_2: 0, C_3H_6: -0.3, C_3H_6O: -0.1, CO_2: 0, H_2O: -0.2) were similar to those measured on Au-DP/TS-1 (H_2: 0.9, O_2: 0.3, C_3H_6: -0.3, C_3H_6O: 0, CO_2: 0, H_2O: -0.1), a decrease in activation energy from approximately 30 kJ mol^{-1} for Au-DP/TS-1 to 4-5 kJ mol^{-1} for Au-PVP/TS-1 suggests there is a change in rate-limiting step and/or active site for hydrogen oxidation. Additionally, an active site model was developed which determines the number of Ti within an interaction range of the perimeter of extracrystalline Au nanoparticles (i.e., the number of Au-Ti active site pairs). This model was used to estimate catalytic turnover frequencies over solely proximal Au-Ti pairs, assuming that hydrogen peroxide does not desorb and migrate from Au sites to Ti sites and instead propylene oxide forms in a concerted mechanism previously termed the "simultaneous" mechanism. Turnover frequencies estimated for this active site model for a dataset containing both Au-DP/TS-1 and Au-PVP/TS-1 were ~20x higher than the highest previous reported estimates (~80 s^{-1} vs. 1-5 s^{-1} at 473 K) for catalytic oxidation on noble metals, suggesting that the simultaneous mechanism occurring over proximal Au-Ti sites alone is incapable of explaining the observed rate of propylene epoxidation and that short-range migration of hydrogen peroxide is kinetically relevant. The agreement of reaction orders, activation energy, and active site model for propylene epoxidation on both Au-DP/TS-1 and Au-PVP/TS-1 suggests a common mechanism for propylene epoxidation on both catalysts containing small intraporous gold clusters and catalysts with exclusively larger extracrystalline gold nanoparticles. Rates of hydrogen oxidation were found to vary proportionally to the amount of surface gold atoms. This is also consistent with the hypothesis that the observed decrease in hydrogen efficiency and PO site-time-yield per gold mass with increasing gold loading are driven primarily by the gold dispersion in Au/TS-1 catalysts.

INTRODUCTION

Propylene oxide (PO) is an important chemical intermediate used in the manufacture of a variety of industrial and consumer products, such as polyurethanes and functional fluids.[1] However, current industrial processes for the production of PO, such as hydrochlorination, hydrogen peroxide to propylene oxide (HPPO), or epoxidation with organic peroxides, all have significant drawbacks, including generation of environmentally harmful byproducts, low selectivity to PO, or the requirement for expensive liquid-liquid separations.[2,3] An opportunity to address these challenges exists in the form of a highly selective gas phase epoxidation reaction, with water as the only major byproduct, using co-fed propylene, hydrogen, and oxygen over gold- and titanium-containing catalysts, as first reported by Haruta and co-workers in the late 1990s.[4] While these catalysts present a unique opportunity, their integration into industrial processes has lagged due to low site-time yield (STY), low hydrogen efficiency, and poor stability with time on stream.

Efforts to increase the active site density and stabilize active sites remain hindered by a lack of fundamental understanding of the reaction kinetics and active site requirements, specifically for the gold

species in the active sites. Earlier studies focused on the importance of titanium dispersion in support materials, where gold supported on Al-free MFI with framework titanium heteroatoms (TS-1), prepared by deposition-precipitation (DP) (Au/TS-1), was observed to consistently give higher STY per catalyst mass (10/10/10/70 mol% $C_3H_6/H_2/O_2/N_2$, 473 K, 101.3 kPa) than other gold-loaded titanium-containing materials tested, such as Au supported on crystalline mesoporous and amorphous Ti-SiO_2.[5–9] Others have endeavored to determine if an optimal gold nanoparticle size exists (i.e., a size which minimizes both direct hydrogen oxidation and unselective propylene oxidation reactions), using both experimental and computational techniques; such efforts resulted in a general agreement that smaller gold nanoparticles or clusters were correlated with increased STY per TEM-derived gold surface area or catalyst mass, however no optimal size was identified.[10–16]

Lee et al. later observed a continuous decrease in PO rate normalized to gold mass, PO selectivity, and hydrogen efficiency with increasing gold loading.[17] Lee et al. also observed a PO rate normalized to TS-1 mass in a core/shell catalyst consisting of a TS-1 core surrounded by an S-1 shell which was then gold loaded via DP, approximately four times greater than of a conventional Au/TS-1 catalyst with the same gold and titanium composition.[18] These results implied that active sites that include small gold clusters inside the micropores of TS-1 are the predominant PO active sites. However, the origin of this kinetic variation with gold loading, be it an intrinsic cluster size effect or merely improved Au dispersion, has not been conclusively determined. These results, in conjunction with kinetic data consistent with a two-site 'simultaneous' mechanism requiring Au-Ti proximity, imply that in addition to large gold nanoparticles observable via TEM on extracrystalline TS-1 surfaces, some fraction of the gold deposited on TS-1 by DP exists as small, intraporous clusters in proximity to intraporous Ti sites.[19,20] Such intraporous gold clusters have been studied by Bukowski et al., elucidating the role of the TS-1 support as a kinetic trap for small gold clusters.[21] Efforts to restrict active sites to the micropores of TS-1 resulted in the synthesis of gold nanoparticles encapsulated in TS-1, however comparisons of this catalyst's performance to Au/TS-1 prepared by DP are difficult because of the authors' use of O_2/H_2O reactants instead of O_2/H_2.[22]

Harris et al. determined that mechanisms requiring an equilibration with gas phase hydrogen peroxide produced in situ were inconsistent with the measured reaction orders in oxygen and hydrogen (H_2: 1 ± 0.2, O_2: 0.4 ± 0.06, 473 K, 101.3 kPa, 2.5-10 mol% O_2, 2.5-10 mol% H_2), while a simultaneous mechanism in which intact hydrogen peroxide diffusion is unnecessary due to proximity between Au and Ti sites could not be ruled out by these measurements.[20] These results suggested that gold and Ti sites located in close proximity are necessary for PO production under the reaction conditions used (473 K, 101.3 kPa, 10/10/10/70 mol% $C_3H_6/H_2/O_2/N_2$, 14,000 $cm^3\ g_{cat}^{-1}\ h^{-1}$). However, due to the lack of control of Au location when DP is used to deposit gold on TS-1, the catalytic contributions of intraporous gold clusters could not be distinguished from those of extracrystalline gold nanoparticles too large to fit into the pores of TS-1 (i.e., those > ~0.6 nm).

Here, we aim to independently elucidate the catalytic roles of both extracrystalline gold nanoparticles and intraporous gold clusters for both hydrogen oxidation and propylene epoxidation, by preparing Au-TS-1 catalysts using PVP-ligated Au nanoparticles (Au-PVP/TS-1) deposited onto TS-1 supports, with initial nanoparticle sizes too large to enter the micropores of TS-1 (≥1 nm diameter) prior to ligand removal. We report apparent activation energies and reaction orders for hydrogen oxidation and intrinsic activation energies and reaction orders for propylene epoxidation, measured on both Au-PVP/TS-1 and Au/TS-1 prepared with DP (Au-DP/TS-1), as well as apparent propylene epoxidation reaction orders on Au-PVP/S-1. We evaluate active site models which assume, respectively, that corner, edge, terrace, perimeter, and all surface Au atoms are active sites for propylene epoxidation. We also evaluate a model assuming gold nanoparticles are spherical and non-faceted. Finally, we use an active site model which estimates the number of externally-accessible Ti-containing active sites within a specified interaction range of a gold nanoparticle perimeter, herein referred to as the 'proximal Ti' model.

We report that the kinetics of propylene epoxidation measured on both Au-PVP/TS-1 and Au-DP/TS-1 agree within error, suggesting that no significant differences in catalytic properties, exist when comparing PO active sites containing small intraporous gold clusters and sites containing large extracrystalline gold nanoparticles. The kinetics of hydrogen oxidation differ significantly between Au-DP/TS-1 and Au-PVP/TS-1 catalysts, suggesting a change in rate-determining step, reaction barrier, or active site. Additionally, rates of propylene epoxidation and hydrogen oxidation follow different trends when comparing rates normalized by either gold mass or average gold nanoparticle diameter, consistent with our previous results that suggested active sites for propylene epoxidation and hydrogen oxidation were distinct.[20] This finding suggests that there are distinct active sites for propylene epoxidation and hydrogen oxidation, which likely consist of different regions of the same Au nanoparticles.

EXPERIMENTAL METHODS

TS-1 and S-1 Synthesis. Synthesis of TS-1 was performed according to previously reported procedures.[23] Briefly, synthesis began by mixing 3.85 g of polyoxyethylene 20-sorbitan monolaurate (Tween 20, Fischer Scientific, enzyme grade) and 61.56 g of deionized water (DI water) (Millipore, Synergy UV Water Purification System, 18.2 MΩ/cm resistivity) and stirring (5 Hz) for 900 s at ambient temperature. Then, 29.38 g of tetrapropylammonium hydroxide (TPAOH, Alfa Aesar, 40 wt%) and 70.00 g of tetraethylorthosilicate (TEOS, Sigma Aldrich, 98%) were added, followed by stirring (5 Hz) under ambient conditions for 1–2 h. In a separate 15 cm^3 disposable centrifuge tube (VWR, sterile polypropylene), 1.14 g of titanium (IV) butoxide (TBOT, Alfa Aesar, 99%+) and 17.26 g of isopropyl alcohol (IPA, Sigma Aldrich, 99.5%) were combined and stirred with a vortex mixer (VWR Mini Vortex Mixer) and subsequently added dropwise to the synthesis gel, with stirring (5 Hz), under ambient conditions. The final molar ratio of the synthesis gel was 1 SiO_2/0.01 TiO_2/0.17 TPA^+/13.1 H_2O/0.0093 Tween 20/0.04 $C_4H_{10}O$/0.85 C_3H_8O. The solution was then stirred (6 Hz), for at least 1 h at 313–318 K before addition to a Teflon-lined stainless-steel autoclave (45 cm^3, Parr Instrument Company model 4744) and placement in an isothermal oven (Yamato DKN402C Constant Temperature Oven) and heated without agitation at 413 K for at least 18 h. The resulting solid was separated from the slurry via centrifugation (Thermo Scientific Heraeus Megafuge 16, 83 Hz for 1800 s), and then washed twice with DI water, twice with acetone (Sigma Aldrich, 99.5%+), and once more with DI water, with each wash using 15 cm^3 of DI water or acetone per gram of TS-1 and a

vortex mixing time of ~30 s. Once washed, the solid was dried for approximately 48 h at 363 K. The dried TS-1 was then treated in flowing air (100 cm^3 min^{-1} g_{cat}^{-1}) at 853 K for 10 h (0.0167 K s^{-1} ramp).

S-1 synthesis was performed identically to TS-1 synthesis, except that the additions of titanium(IV) butoxide and isopropyl alcohol were omitted.

Preparation of Au-PVP/TS-1 and Au-PVP/S-1 Catalysts. Polyvinylpyrrolidone (PVP) coated gold nanoparticles (Au-PVP) were deposited using the incipient wetness impregnation (IWI) method onto TS-1 and S-1 supports, as described in previous reports.[24,25] A typical aqueous solution of Au-PVP was prepared by dissolving 0.02 g of hydrogen tetrachloroaurate(III) trihydrate ($HAuCl_4 \cdot 3H_2O$, Alfa Aesar, 99.99% (metals basis)) in 50 g of DI water (Millipore, Synergy UV Water Purification System, 18.2 MΩ/cm resistivity). Then, 555 mg of PVP (40 kDa, Sigma-Aldrich) were added with stirring (5 Hz) before the mixture was placed in a 273 K bath and stirred for an additional 1800 s. Next, 5 cm^3 of a 0.1 M aqueous solution of sodium borohydride ($NaBH_4$, Sigma-Aldrich, 99.99% (trace metals basis)) were rapidly added to the solution while stirring at 273 K was continued. The resulting solution was then used for IWI of the TS-1 or S-1 support, followed by drying of the resulting Au-PVP/TS-1 or Au-PVP/S-1 in a vacuum oven overnight (>8 h, 298 K, 15 kPa). Due to the low concentration of gold in the Au-PVP solution, the IWI and vacuum drying procedures were repeated until the target gold loading was reached, which was then confirmed by elemental analysis.

Catalyst Characterization. Powder X-ray diffraction (XRD) patterns were collected using a Rigaku Smartlab X-ray diffractometer equipped with an ASC-6 automated sample changer stage and a Cu Kα X-ray source (1.76 kW). A typical measurement procedure consisted of packing ~0.01 g of sample into a zero-background, low dead-volume sample holder (Rigaku), then scanning a 2θ range of 4-40° at a scan rate of 0.000417° s^{-1} with a step size of 0.02°.

Nitrogen adsorption isotherms (77 K) were measured using a Micromeritics 3Flex Surface Characterization Analyzer. Prior to measuring isotherms, samples (~0.05 g, sieved to 180-250 μm particle diameter) were degassed under vacuum (<0.005 Torr) with heating to 393 K (0.0167 K s^{-1}) for 2 h, followed by heating to 623 K (0.0167 K s^{-1}) for 8 h. Micropore volumes were determined using a semi-log derivative analysis of N_2 isotherms ($\delta(V_{ads}/g)/\delta(\log(P/P_0))$ vs $\log(P/P_0)$) to identify the end of micropore filling.

Bulk elemental compositions were determined using either atomic absorption spectroscopy (AAS) using a PerkinElmer model AAnalyst 300 or inductively coupled plasma optical emission spectroscopy with a Perkin Elmer ICP-OES (Thermo Scientific iCAP 7000 Plus Series ICP-OES). 1000 ppm standards (Sigma Aldrich TraceCERT) were used to create a series of diluted calibration standards, which were used to calibrate the instrument prior to measurement for each element. To prepare the samples for ICP-OES analysis, Au/TS-1 and Au/S-1 samples (~0.10 g) were dissolved in 2 g of HF (48 wt%, Alfa Aesar) and 2.5 g of aqua regia (prepared from a 2:1 v/v ratio of 37 wt% HCl, Mallinckrodt Chemicals, and 70 wt% HNO_3, Mallinckrodt Chemicals) overnight before being diluted with 30 g of DI water. For elemental analysis with ICP-OES, samples were further acidified with 2.5 g of HNO_3 (70 wt%, Sigma Aldrich) before analysis. Titanium content was measured after calcination but before gold deposition. The Si/Ti ratio for each sample was calculated from the titanium mass fraction and the unit cell formula for the TS-1 zeotype.

Diffuse reflectance UV-Vis (DRUV-Vis) spectra were collected using a Varian Cary 5000 UV-Vis-NIR equipped with a Harrick Praying Mantis *in situ* diffuse reflectance cell. Spectra were collected at a rate of 10 nm s^{-1} on samples: (i) first exposed to ambient conditions and held in dry flowing helium 4.17 cm^3 s^{-1} (g sample)$^{-1}$) (referred to as "ambient spectra") and (ii) after subsequent treatment to 523 K (0.167 K s^{-1}) for 1 h in dry flowing helium (4.17 cm^3 s^{-1} (g sample)$^{-1}$) (referred to as "dehydrated spectra"). Poly(tetrafluoroethylene) (PTFE, 1 μm powder, Sigma Aldrich) was used as a 100% reflectance standard, which then allowed conversion of the reflectance spectrum to an adsorption spectrum using the Kubelka-Munk (F(R)) function. Adsorption edge energies were calculated from the x-intercepts of Tauc plots ($[F(R)h\nu]^2$ vs. $h\nu$).[26–28]

Thermogravimetric analysis (TGA) experiments were performed on a TA instruments SDT Q600 thermogravimetric analyzer and differential scanning calorimeter (TGA-DSC) by heating ~0.02 g of as-made Au-PVP/TS-1 or Au-PVP/S-1 in 83.3 cm^3 s^{-1} g_{cat}^{-1} dry air (Indiana Oxygen, air zero grade, < 1 ppm total hydrocarbon content) to 423 K and holding for 2 h to remove any physisorbed water before further heating in air. To determine total PVP content, samples were heated to 1073 K (0.17 K s^{-1}) and held for 0.5 h. Combustion of PVP was characterized by a pair of exotherms and mass losses, centered at 625 K and 770 K, respectively.

Transmission electron microscopy (TEM) and high-angle annular dark-field scanning transmission electron microscopy (HAADF-STEM) images were obtained on an FEI Talos F200X S/TEM with a 200kV X-FEG field-emission source. To prepare TEM samples, Au-PVP/TS-1 samples were sonicated in acetone and then drop-casted onto a carbon-coated Cu grid (Ted Pella).

Kinetic Testing. Kinetic data for the gas-phase reactions examined herein were measured in an automated recycle reactor operated as a continuous stirred tank reactor (CSTR), which eliminates concentration gradients throughout the catalyst bed under all feed conditions and reactant conversions. Details of the reactor system, including details of the automation, can be found in the supplemental information (Figure S.1), as well as in a previous publication.[20]

Kinetic measurements were performed on 0.15 g of as-deposited catalysts after sieving to 125-250 μm particle diameter, loading into a Pyrex U-tube reactor, and installing this reactor in a furnace controlled by a Eurotherm 2408 controller protected by an over-temperature thermocouple and controller (Omega CN9000A). Reaction temperatures were measured by a thermocouple (Omega, K type) housed in a quartz thermowell whose tip was in contact with the radial and axial center of the catalyst bed. The reactor is connected to a circular glass manifold serving as a recirculating volume (Figure S.1) using 0.25" ultra-torr fittings (Swagelok). The top of the reactor and furnace were insulated using fiberglass insulation. A leak check was performed at ambient temperature by pressurizing the reactor and glass manifold to 122 kPa with nitrogen, and the unit was considered leak free when no detectable change in pressure (<0.7 kPa) occurred over a period of 600 s.

For Au-PVP/TS-1 and Au-PVP/S-1 catalysts, flow of air was started (SV = 10,000 cm^3 h^{-1} g_{cat}^{-1}) and the reactor temperature was increased to 573 K (0.017 K s^{-1}). This condition was maintained for 24 h before cooling to 473 K in a nitrogen purge of 0.8 cm^3 s^{-1} and switching to a 3/3/94 mol% $H_2/O_2/N_2$ flow (SV = 10,000 cm^3 h^{-1}

g_{cat}^{-1}). Care was taken to stay below the flammable regime of $H_2/O_2/N_2$ mixtures, as well as to avoid reaching the saturation pressure of water under ambient conditions. This condition was held until 12 h after the rate of hydrogen consumption reached steady state, typically about 48 h.

Kinetic experiments were performed by independently varying the flowrates of propylene, hydrogen, or air while maintaining a constant total flowrate by adjusting the nitrogen flowrate, following an activation procedure. The activation procedure for both Au-PVP/TS-1 and Au-DP/TS-1 catalysts consisted of exposing the pre-catalysts to reaction gases (10/10/10/70 mol% $C_3H_6/H_2/O_2/N_2$, 101.3 kPa, 14,000 $cm^3\ h^{-1}\ g_{cat}^{-1}$) beginning at ambient temperature and ramping to the initial reaction temperature of 473 K (0.0167 K s^{-1}). Catalysts were then held at these conditions until a steady state was achieved for both the propylene epoxidation and hydrogen oxidation rates. Propylene oxide and carbon dioxide co-feed experiments were performed using gases fed by digital mass flow controllers from a CO_2 (Indiana Oxygen) cylinder and a 1% PO/N_2 cylinder (Airgas, 1 ± 0.02% PO in N_2, certified standard grade), while water co-feed experiments were performed by flowing N_2 from a digital mass flow controller through a vapor-liquid-equilibrium saturator whose temperature was monitored by a thermocouple which was mounted in a quartz thermocouple well filled with water and sealed with parafilm. To avoid flammable or explosive gas mixtures, concentrations of propylene, hydrogen, and oxygen were decreased from the standard 10 mol% in a non-monotonic fashion. Apparent activation energy measurements were performed starting from the standard 473 K condition and varying the temperature in a non-monotonic fashion in the range 443-483 K. For both apparent reaction order and apparent activation energy experiments, a minimum of three repeated GC injections was taken at each condition and the reported data represent the average of the last two, or more, of these injections.

Products were injected into an on-line Agilent 6890 GC. C_2 and C_3 hydrocarbon products were quantified with a Supelcowax-10 capillary column (Agilent, 60 m x 530 μm, 1 μm film thickness) connected to a flame-ionization detector (FID). CO_2, O_2, and H_2 were quantified with a 60/80 Chromosorb 102 packed column connected to a thermal conductivity detector. Both columns and detectors used N_2 as the carrier gas. GC peak areas were quantified using (2) pre-measured response factor calibrations for propylene, propanal, ethanal, acetone, acrolein, and propylene oxide on the FID, and H_2, O_2, and CO_2 for the TCD. Propylene conversions calculated based on the decrease in the effluent propylene concentration were typically less than 5%, which is within the uncertainty of the instrument. As a result, reported propylene conversions (X_{C3H6}) were calculated as the moles of C_3 in the products divided by the moles of C_3H_6 in the feed (Eq. 1):

$$X_{C_3H_6} = \frac{moles\ C_3 in\ products}{moles\ C_3\ in\ feed} \quad (1)$$

The product carbon selectivity for each carbon-containing product was defined as:

$$S_{c,i} = \frac{(moles\ product\ i\ formed)x(C\ atoms\ in\ product\ i)}{total\ moles\ C\ in\ all\ products} \quad (2)$$

the hydrogen selectivity was defined as:

$$S_{H_2} = \frac{moles\ PO\ formed}{moles\ H_2\ consumed} \quad (3)$$

and the rate of hydrogen oxidation is calculated as:

$$r_{H_2O} = \frac{(moles\ H_2\ consumed) - (moles\ PO\ formed)}{g_{cat} \cdot s} \quad (4)$$

assuming one mole of hydrogen is consumed in water formation per mole of propylene oxide formed, according to the overall reaction for PO formation (Eq. 5).

$$C_3H_6 + H_2 + O_2 \rightarrow C_3H_6O + H_2O \quad (5)$$

RESULTS AND DISCUSSION

Characterization of Titanosilicate-1 and Silicate-1. Structural characterization data (XRD, N_2 micropore, UV-Vis spectroscopy)

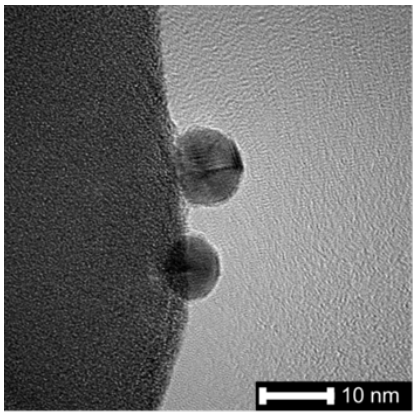

Figure 1: TEM micrograph of gold nanoparticles on 0.082Au-PVP/S-1, after kinetic experiments. The scale bar represents 10 nm.

for the TS-1 and S-1 samples used in this report can be found in figures S.2-S.5. XRD patterns were consistent with those reported for titanium MFI zeotypes previously.[17,20] The lack of splitting of the peak at 2θ = 24.6° indicates the presence of the orthorhombic unit cell(see Figure S.2b).[29] Nitrogen adsorption isotherms for TS-1 and S-1 samples were typical of the MFI structure, and micropore volumes were consistent with values typically reported for TS-1 (micropore volumes: 0.16-0.18 $cm^3\ g^{-1}$).[17,20,30]

DRUV-Vis spectra indicated the presence of primarily isolated Ti^{4+} sites in TS-1. DRUV-Vis peak centers were between 220 nm and 230 nm (Figure S.4), which is consistent with values reported previously for dehydrated, isolated Ti^{4+} in TS-1 as well as Ti-Beta-F zeolites.[17,20,31] The edge energies calculated from DRUV-Vis spectra for dehydrated TS-1 samples are all greater than 4.9 eV (Tauc plots shown in Figure S.5, edge energies reported in Table S.1), which is characteristic of samples with primarily isolated, tetrahedrally coordinated Ti^{4+} sites. However, the existence of a minor fraction of the Ti in small, octahedrally coordinated TiO_2 domains cannot be ruled out, as the edge energies of such domains increases with decreasing size due to quantum confinement effects.[32] The presence of TiO_2 domains larger than three nanometers can be ruled out by the lack of distinct peaks in X-ray diffractograms at 25.7°, 27.9°, and 31° for TS-1(73) and TS-1(126) (Figure S.2).[33,34] The gold nanoparticles on Au-PVP catalysts used in this work had similar geometries and particle size distributions to one another. For all samples used in this study, the gold nanoparticles have a size distribution centered around particles of 6 – 8 nm in diameter (Figures 1, 2, S.11-S.14), with number averages and standard deviations shown in Table 1.

***In Situ* Removal of PVP Ligands.** PVP ligands were removed with a combination of *in situ* treatments, and their absence was

confirmed with a combination of TGA and TEM data. Figures 3a and 3b show TGA mass loss and heat flow data, respectively, for as-made (solid line), post-air treatment (long dashes), and air and $H_2/O_2/N_2$-treated (short dashes) samples. The air treatment consisted of flowing dry air at a space velocity of 10,000 $cm^3\ g_{cat}^{-1}\ h^{-1}$ and temperature of 573 K. These

Table 1: Gold nanoparticle number average diameters and standard deviations calculated from TEM-derived particle size distributions for all samples used in this study. Particle size distributions were measured after air treatment, $H_2/O_2/N_2$ treatment, and the conclusion of all kinetic experiments for all samples.

Catalyst	Average diameter [nm]
0.083Au-PVP/TS-1(126)	7.6 ± 3.3
0.083Au-PVP/TS-1(126), repeat	6.5 ± 2.9
0.082Au-PVP/S-1	6.6 ± 2.5
0.11Au-PVP/TS-1(73)	7.4 ± 2.9

conditions were chosen because a 'light off' temperature of approximately 573 K for Au-PVP samples was observed in an initial TGA experiment with as-made 0.083Au-PVP/TS-1(126) (Figure S.7). The conditions for the $H_2/O_2/N_2$ treatment were a mixture of 3/3/94 mol% $H_2/O_2/N_2$ at the same space velocity and a temperature of 473 K. These conditions were chosen based on previous experiments showing CO_2 evolution on Au-DP/TS-1 samples at 473 K flowing only $H_2/O_2/N_2$ after flowing $C_3H_6/H_2/O_2/N_2$ at 473 K (Figure S.6) and because they are close to the conditions used for measurement of propylene epoxidation rates. The data from TGA measurements on all samples (Figure 3a) shows a rapid loss of mass in the temperature range 320-420 K corresponding to approximately 5% of the total sample masses. The heat flow data for all samples (Figure 3b) show an endothermic feature in the same temperature range, thus these features are attributed to water desorption. In the sample mass data for the as-made Au-PVP/TS-1 two additional mass losses are observed in the range 500 – 800 K sample (Figure 3a, dashed-dotted line). These mass losses correspond to a pair of exothermic features in the heat flow data (Figure 3b, dashed-dotted line) over the same temperature range, the first centered at approximately 625 K and the second centered at approximately 770 K. The feature centered at 625 K can be attributed to thermal degradation of any inorganic salts and of PVP to a carbonaceous overlayer and lower molecular weight volatile species, while the feature centered at 770 K can be attributed to oxidation of the remaining carbonaceous species.[35] The air-treated Au-PVP/TS-1 sample (Figure 3, long

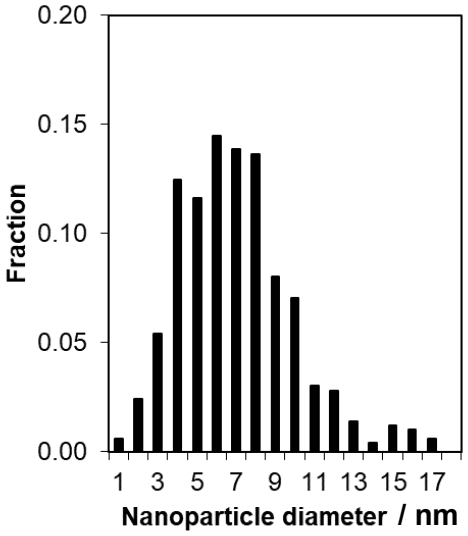

Figure 2: Gold nanoparticle size distribution, measured from TEM micrographs taken on 0.083Au-PVP/TS-1(126) after kinetic experiments. The number average gold nanoparticle diameter is 6.5 ± 2.9 nm and the distribution is based on a count of 498 gold nanoparticles.

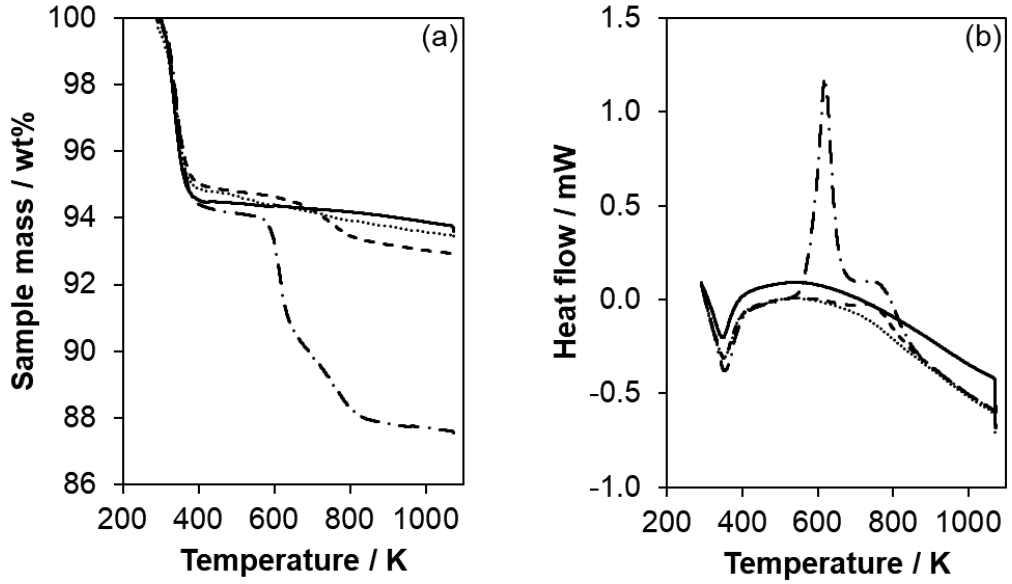

Figure 3: Sample mass (a) and heat flow (b) over the course of a TGA experiment. Calcined TS-1(126) (solid line), as-made 0.083Au-PVP/TS-1(126) (dash dot), post-air treatment (long dashes), and air and $H_2/O_2/N_2$-treated 0.083Au-PVP/TS-1(126) (dots) catalysts were held at ambient temperature with 1.67 $cm^3\ s^{-1}$ of dry air flowing for 900 s before ramping to 1073 K (10 K/min) and holding for 1800 s. The strong negative trend in the heat flow at high temperature is an artifact of the instrument.

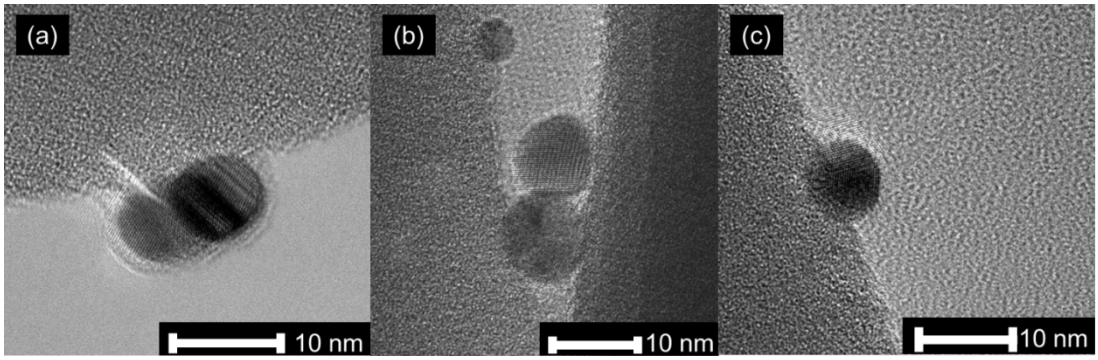

Figure 4: HRTEM micrographs of typical gold nanoparticles on (a) 0.08 Au-PVP/TS-1(126) after treatment in air and $H_2/O_2/N_2$, (b) 0.11Au-PVP/TS-1(73) after treatment in air and $H_2/O_2/N_2$ as well as an activation period in $C_3H_6/H_2/O_2/N_2$ (Figure 5) , and (c) 0.08Au-PVP/TS-1(126) after all three treatments (air, $H_2/O_2/N_2$, and an activation period in $C_3H_6/H_2/O_2/N_2$) and the conclusion of all kinetic experiments. The scale bars represent 10 nm.

dashes) lacks the initial mass loss and exothermic feature in the 500 – 800 K temperature range, however the second mass loss and exothermic feature centered at approximately 780 K are both observed. In the data for the post-$H_2/O_2/N_2$ treated Au-PVP/TS-1 sample (Figure 3, dots), neither of the features in the 500 – 800 K range associated with PVP decomposition and combustion is observed.

TEM images of the air-treated and post-$H_2/O_2/N_2$ treated Au-PVP/TS-1 samples were also used to track the progress of PVP removal from the catalyst surface. They reveal the presence of a 1-2 nm thick layer primarily covering the gold nanoparticles. This overlayer is likely carbon from thermal PVP decomposition, due to the lack of regular atomic spacing and lesser intensity in the HRTEM images, both of which are consistent with an amorphous carbon-rich overlayer. An additional pretreatment under a standard set of reaction conditions (10/10/10/70 mol% $C_3H_6/H_2/O_2/N_2$, 14,000 $cm^3\ h^{-1}\ g_{cat}^{-1}$ SV, and 473 K), removed this overlayer (Figure 4). The rate of propylene epoxidation during this final treatment slowly increased until it plateaued at a maximum value (~7 $g_{PO}\ h^{-1}\ kg_{cat}^{-1}$) after approximately 15 ks (Figure 5), which is consistent with the catalyst undergoing some structural or chemical change, such as loss of any remaining surface-bound species and/or rearrangement due to sintering. Further TEM images (Figure 4c) do not show an overlayer, although we cannot rule out the presence of minute amounts of adatoms bound to gold surfaces. Although none was observed, any remaining carbon can also not be distinguished from carbon deposited during the propylene epoxidation reaction.

After development of the pretreatment procedures for removal of PVP ligands, as discussed above, a typical Au-PVP/TS-1 or Au-PVP/S-1 catalyst considered here was exposed to the following sets of conditions: i) 573 K flowing dry air (10,000 $cm^3\ h^{-1}\ g_{cat}^{-1}$) for 24 hours, ii) 473 K flowing $H_2/O_2/N_2$ (3/3/94 mol% $H_2/O_2/N_2$, 10,000 $cm^3\ h^{-1}\ g_{cat}^{-1}$) for 48 hours, and iii) a reaction mixture of $C_3H_6/H_2/O_2/N_2$ (10/10/10/70 mol% $C_3H_6/H_2/O_2/N_2$, 14,000 $cm^3\ h^{-1}\ g_{cat}^{-1}$) at 473 K. This final condition was held until the rates of propylene epoxidation and hydrogen oxidation reached steady-state (Figure 5). After these three sets of pretreatment conditions were used, the kinetic experiments were conducted.

Propylene Epoxidation Reaction Kinetics on Au-PVP/TS-1 and Au-PVP/S-1. Measurement of reaction orders and activation energies was performed after *in situ* removal of PVP ligands. Internal and external mass transfer limitations were estimated to be negligible by calculation of the Mears criterion (<< 0.15, Section S.5) and the Thiele modulus (between 10^{-2} and 10^{-3}, Section S.5), and internal mass transfer limitations for Au-PVP/TS-1 catalysts would be expected to be negligible given the location of gold nanoparticles on external crystallite surfaces. The measured reaction orders and activation energy for propylene epoxidation over Au-PVP/TS-1 catalysts were similar to previously reported values over Au-Ti catalysts (Table 2). Reaction orders for oxygen, hydrogen, and propylene, once corrected for the measured PO inhibition (reaction order for PO was -0.6) by multiplication by a factor of 1.6 (see Harris et al.[20]), were 0.5, 1.3, and 0.2, while the activation energy for propylene epoxidation was 51 kJ mol^{-1}.

While the reaction orders and activation energy for propylene epoxidation on Au-PVP/TS-1 catalysts are similar to values reported for conventional Au/TS-1 catalysts prepared by deposition-precipitation and are consistent with a 'simultaneous' mechanism requiring proximity of the Au and Ti active sites, the average value of

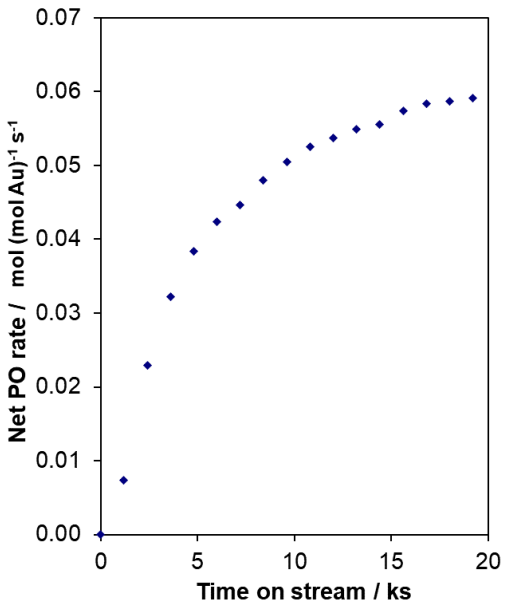

Figure 5: The rate of propylene epoxidation for 0.11Au-PVP/TS-1(73) during the first six hours of reaction time after treatment in air at 573 K and 3/3/94 mol% $H_2/O_2/N_2$ at 473 K. Reaction conditions: 10/10/10/70 mol% $C_3H_6/H_2/O_2/N_2$, T = 473 K, SV = 14,000 $cm^3\ h^{-1}\ g_{cat}^{-1}$, P = 101.3 kPa.

the hydrogen reaction order is greater than one (1.3) and cannot be rationalized in the 'simultaneous' mechanism (Scheme 1) without including a third H_2(g)-derived hydrogen atom in the rate-determining step.[19,20] Alternatively, mechanisms which include a second rate-determining step with three participating H_2(g)-derived hydrogen atoms are consistent with hydrogen reaction orders of up to 1.5; such a mechanism was proposed by Lu et al. that invoked H_2O_2 spillover from Au sites to Ti-OH.[36] Mechanisms such as the one proposed by Lu et al.

1) $2H* \rightleftharpoons H_2 + 2*$

2) $O_2 + * \rightleftharpoons O_2*$

3) $H_2 + O_2* + * \rightleftharpoons HOO* + H*$

4) $O_2 + 2\,H* \rightleftharpoons HOO* + H*$

5) $H_2 + HOO* + * \rightleftharpoons HOOH* + H*$

6) $C_3H_6 + \square \rightleftharpoons C_3H_6\square$

7) $C_3H_6\square + HOOH* + H* \rightarrow C_3H_6O\square + H_2O* + H*$

8) $C_3H_6O + * \rightleftharpoons C_3H_6O*$

9) $C_3H_6O + \square \rightleftharpoons C_3H_6O\square$

10) $H_2O + * \rightleftharpoons H_2O*$

Scheme 1: Proposed series of elementary steps for propylene epoxidation on Au/TS-1 catalysts known as the 'simultaneous' mechanism.[19,20] * is an Au site and □ is a Ti site and they are assumed to be in proximity, such that a gold-adsorbed HOOH and titanium-adsorbed propylene can react to form propylene oxide.

are consistent with this requirement for explaining hydrogen reaction orders greater than unity for propylene epoxidation due to the inclusion of a second rate-determining step with three H_2 (g)-derived hydrogen atoms (Eq. H-4, [36]).[36]

The rate of propylene epoxidation on 0.082Au-PVP/S-1 is 5-10% of the rate on Au-PVP/TS-1 catalysts, or roughly 1% of the rate on Au-DP/TS-1, or 10% of the rate on 0.083Au-PVP/TS-1(126) (Table 3). However, the rates of unselective C_1-C_3 byproduct production on 0.083Au-PVP/TS-1(126) and 0.082Au-PVP/S-1 are identical within error (Table 3), implying PO and C_1-C_3 byproducts are produced in parallel reaction pathways. The kinetics of propylene epoxidation on Au-PVP/S-1 are markedly different from those measured on Au-PVP/TS-1 and Au-DP/TS-1 (Table 2), which suggests the existence of secondary site(s) on gold surfaces and/or the gold-support interface capable of catalyzing propylene epoxidation by a reaction mechanism that differs from that over catalysts that contain both Au and Ti. The PO reaction order for propylene epoxidation over Au-PVP/S-1 was not able to be measured due to apparent negative rates of propylene epoxidation upon co-feeding PO (Figure S.8), presumably due to reactions of PO to form other products, although this reaction pathway was not investigated here.

Hydrogen Oxidation Reaction Kinetics on Au-PVP/TS-1 and Au-PVP/S-1. The kinetics of hydrogen oxidation were measured simultaneously with the kinetics of propylene epoxidation. The rate of direct hydrogen oxidation (i.e., H_2 consumption beyond the one mol H_2 consumed per mol PO produced) was measured indirectly according to equation 4, due to our inability to directly measure effluent water concentrations via GC. Our inability to measure gas-phase water concentrations is because the thermal conductivity of air saturated with water (298 K, 101.3 kPa) is nearly identical to the thermal conductivity of the GC carrier gas, N_2, used here.[37] Equation 4 assumes that all hydrogen consumed in excess of the PO produced forms water, which is consistent with our observation of the absence of any other species to which hydrogen could go to (e.g., alcohols, saturated hydrocarbons) in the reactor effluent.

$$r_{H_2O} = \frac{kK_{OOH}K_{O_2}P_{O_2}\sqrt{K_{H_2}P_{H_2}}P_{H_2}}{(1+\sqrt{K_{H_2}P_{H_2}}+K_{O_2}P_{O_2}+K_{OOH}K_{O_2}P_{O_2}\sqrt{K_{H_2}P_{H_2}})(1+\sqrt{K_{H_2}P_{H_2}})}$$

Table 2: Reaction orders and activation energies for propylene epoxidation on 0.083Au-PVP/TS-1 and 0.082Au-PVP/S-1 compared with previously reported values for Au/TS-1 prepared with deposition precipitation. Reaction conditions: 2.5-10/2.5-10/2.5-10/bal. mol% $C_3H_6/H_2/O_2/N_2$, SV = 26,000 $cm^3\,h^{-1}\,g_{cat}^{-1}$, T = 473 K (443-483 K for E_{app}), P = 101.3 kPa.

Catalyst	Reaction orders						E_{app}
	H_2	O_2	C_3H_6	PO	CO_2	H_2O	kJ mol^{-1}
Au-DP/TS-1 [a, b]	1 ± 0.2	0.4 ± 0.1	0.4 ± 0.1	-0.6 ± 0.2	0	0	52 ± 6
Au-PVP/TS-1 [a, c]	1.3 ± 0.2	0.5 ± 0.1	0.2 ± 0.1	-0.6 ± 0.1	0	0	51 ± 4
Au-PVP/S-1 [d]	0.6 ± 0.1	0.4 ± 0.1	0.5 ± 0.1	--[e]	0	0.7 ± 0.1	3 ± 3

[a] Reactant orders and E_{app} corrected by a factor of (1-d), where d is the PO order,

[b] Kinetic parameters from Harris et al.[20] Values are averages over eight separate ca

[c] Average values from two separate sets of kinetic experiments using 0.083Au-PV

[d] Not corrected for inhibition.

[e] PO order for PO production not able to be measured due to excessive PO consu

Table 3: Comparisons of catalytic STY of propylene epoxidation, unselective hydrogen oxidation (Eq. 4), and total C_1-C_3 byproduct generation on 0.11Au-PVP/TS-1(73), 0.083Au-PVP/TS-1(126) (averaged over two sets of experiments), and 0.082Au-PVP/S-1. Reaction conditions: 10/10/10/70 mol% $C_3H_6/H_2/O_2/N_2$, SV = 14,000 $cm^3\ h^{-1}\ g_{cat}^{-1}$, T = 473 K, P = 101.3 kPa.

	Site-Time Yields		
	C_3H_6 epoxidation	H_2 oxidation	Total C_1-C_3 byproducts
Catalyst	$g_{PO}\ h^{-1}\ kg_{cat}^{-1}$	$\mu mol_{H2}\ s^{-1}\ g_{cat}^{-1}$	(mol C_3) $h^{-1}\ kg_{cat}^{-1}$
0.11Au-PVP/TS-1(73)	7	0.22	0.53
0.083Au-PVP/TS-1(126)	11	0.83	0.11
0.082Au-PVP/S-1	0.4	1.2	0.095

Scheme 2: Dual-site reaction mechanism for hydrogen oxidation on gold nanoparticles, proposed by Barton and Podkolzin.[16] ∗ represent Au sites accessible to all species, and □ represent Au sites accessible only to hydrogen. Reproduced from Barton and Podkolzin, J. Phys. Chem. B 2005, 109, 6, 2262-2274. Copyright 2005 American Chemical Society.

1) $O_2 + * \rightleftharpoons O_2*$

2) $H_2 + 2* \rightleftharpoons 2H*$

3) $H_2 + 2\square \rightleftharpoons 2H\square$

4) $O_2* + H\square \rightleftharpoons HOO* + \square$

5) $HOO* + H_2 + \square \rightarrow HOOH* + H\square$

The kinetics of hydrogen oxidation on Au-PVP catalysts differ from those previously reported for Au/TS-1 prepared by DP, for both feeds containing propylene and feeds containing only hydrogen, nitrogen, and oxygen (Table 4). While direct hydrogen oxidation reaction orders measured on Au-PVP/TS-1 (H_2: 0.8, O_2: 0, C_3H_6: -0.3, PO: -0.1, CO_2: 0, H_2O: -0.2) and Au-PVP/S-1 (H_2: 0.9, O_2: 0, C_3H_6: -0.2, PO: -0.1, CO_2: 0, H_2O: -0.3) are similar, the rate of hydrogen oxidation on both Au-PVP/TS-1 and Au-PVP/S-1 catalysts is relatively insensitive to temperature when compared to Au-DP/TS-1 catalysts, which is reflected in the difference in activation energies (4 kJ mol^{-1} versus 30-40 kJ mol^{-1}). This is consistent with a difference in either the reaction barrier, rate-determining step, and/or active site between the smaller gold nanoparticles and clusters on Au-DP/TS-1 catalysts and the larger gold nanoparticles on Au-PVP/TS-1 and Au-PVP/S-1 catalysts discussed here. Additionally, the oxygen reaction order for hydrogen oxidation differs between Au-PVP/TS-1 and Au-DP/TS-1 catalysts (0 and 0.4, respectively), suggesting differences in either coverages of O_2-derived surface species or rate-determining steps (i.e., the rate-determining step for hydrogen oxidation on Au-PVP/TS-1 and Au-PVP/S-1 catalysts differs from that proposed for Au-DP/TS-1 catalysts by Barton and Podkolzin[16] (Scheme 2)).

While the activation energy for hydrogen oxidation on Au-PVP catalysts is significantly lower than values reported for Au-DP catalysts, it is in rough agreement with the activation energy calculated for O_2 adsorption on gold wire by Kul'kova and Levchenko and Choi et al., who estimated values of 13 kJ mol^{-1} and 12 kJ mol^{-1} for this step, respectively, as well as the activation energy for O_2-assisted hydrogen dissociation on Au(211), estimated to be 10 kJ mol^{-1}.[16,38,39] Furthermore, we posit that it is unlikely that there are slower diffusion rates for H_2, O_2, and/or H_2O during H_2 oxidation on Au particles on the external surface of TS-1 than those for H_2 oxidation over Au particles within the micropores of TS-1, as would be required if mass transfer limitations were to explain the observed difference in apparent activation energies. This suggests that either i) the rate-

Table 4: Apparent reaction orders and activation energies for hydrogen oxidation on 0.083Au-PVP/TS-1 and 0.082Au-PVP/S-1 compared with previously reported values for Au/TS-1 prepared with deposition precipitation.

	Reaction orders						E_{app}
Catalyst	H_2	O_2	C_3H_6	PO	CO_2	H_2O	kJ mol^{-1}
Au-DP/TS-1[a]	0.9 ± 0.1	0.3 ± 0.1	-0.3 ± 0.07	0 ± 0.2	0	-0.1 ± 0.07	31 ± 10
0.083Au-PVP/TS-1(126)[b]	0.8 ± 0.2	0 ± 0.2	-0.3 ± 0.2	-0.1 ± 0.1	0	-0.2 ± 0.1	4 ± 1
0.082Au-PVP/S-1[b]	0.9 ± 0.1	0.1 ± 0.1	-0.2 ± 0.1	-0.1 ± 0.1	0	-0.3 ± 0.1	4 ± 1
Au-DP/TS-1[c,d]	0.7 – 0.8	0.1 – 0.2	n.m.[e]	n.m.	n.m.	0	37 – 41

[a] Kinetic parameters from Harris et al. [20]. Values are averages over eight separate catalysts.

[b] Reaction conditions: T = 473 K (443-483 K for E_{app}), 2.5 – 10/2.5 – 10/2.5 – 10/0 – 0.24/0 – 5/0 – 0.3/Bal. mol% $H_2/O_2/C_3H_6/PO/CO_2/H_2O/N_2$, SV = 26,000 $cm^3\ h^{-1}\ g_{cat}^{-1}$, P = 101.3 kPa.

[c] Kinetic parameters from Barton and Podkolzin [16].

[d] Reaction conditions: T = 433 K (383-483 K for E_{app}), 0.5 – 19.7/0.5 – 39.5/0 – 3/Bal. mol% $H_2/O_2/H_2O/N_2$, SV = 15,000 – 150,000 $cm^3\ h^{-1}\ g_{cat}^{-1}$, P = 101.3 kPa.

determining step for hydrogen oxidation on gold surfaces changes as the size of the gold nanoparticle increases, or that ii) the barrier for hydrogen oxidation decreases on larger Au nanoparticles. Additionally, while non-zero hydrogen oxidation reaction orders for oxygen have been reported for Au-DP/TS-1 catalysts, no significant O_2-dependence on the rate of hydrogen oxidation was observed for Au-PVP/TS-1 catalysts, which, in the context of a Langmuir-Hinshelwood type mechanism, suggests that the larger gold nanoparticles present on Au-PVP/TS-1 and Au-PVP/S-1 catalysts have higher coverages of adsorbed oxygen than the gold nanoparticles and small clusters on Au-DP/TS-1 catalysts studied by Harris et al. and by Barton and Podkolzin.[16,20] This can be demonstrated using Eq. 6, derived from the two-site hydrogen oxidation mechanism proposed by Barton and Podkolzin.[16]

Active Site Models and Rate Normalization for Au-DP/TS-1 and Au-PVP/TS-1. To further evaluate the hypothesis that the gold actives sites responsible for propylene epoxidation on Au-DP/TS-1 and Au-PVP/TS-1 catalysts are similar, the rates of propylene epoxidation normalized to estimates of the fraction of gold which is in PO-producing active sites for

several active site models were calculated for each catalyst considered here. Given that the geometry of gold nanoparticles on Au-PVP/TS-1 and Au-PVP/S-1 catalysts studied here was not able to be determined, we cannot propose a new physical model. However, we can use the model of a truncated cubo-octahedron with a Au(111) top facet (Figure S.8) proposed for gold nanoparticles by Feng et al. under propylene epoxidation reaction conditions, which is similar to the model proposed for gold nanoparticles by Williams et al. for gold nanoparticles under water-gas shift reaction conditions, as a basis for comparison.[40–42] Using this physical model in conjunction with TEM-derived gold nanoparticle size distributions and bulk gold loadings, we predicted the functional dependence of the PO rate on the prevalence of each atom type and evaluated the model regressions after minimizing the squared residuals for each case using equations 7 and 8, where r is the experimentally measured rate of propylene epoxidation, C_{site} is a fit parameter which is the rate per site for the site type being considered, s(d) is the number of surface atoms of the given type (e.g., corner atoms) in a given particle, and t(d) is the total number of atoms in a given particle. While these models can be used with nanoparticles of uniform size, to account for the size variation observed with gold nanoparticles on these catalysts, the following process was used to avoid this limitation of our analysis: For each nanoparticle, a TEM-measured diameter was used in conjunction with the nanoparticle models in section S.9 to determine the edge length in atoms that correspond to the measured diameter of each nanoparticle. The relationships in tables S.4 and S.5 were then used to determine the population of each type of atom (e.g., corner, edge, etc.) for each nanoparticle. These counts of atom types were then summed over the entire size distribution for the catalyst being considered. Therefore, this analysis is not limited to considering only one nanoparticle diameter and is representative of the entire measured distribution of nanoparticles.

$$r = C_{site}[\sum s(d) / \sum t(d)] \quad (7)$$

$$min(r - C_{site}[\sum s(d) / \sum t(d)])^2 \quad (8)$$

Models for corner, edge, terrace, surface, and perimeter atoms on a truncated cubo-octahedron with a Au(111) top facet were created

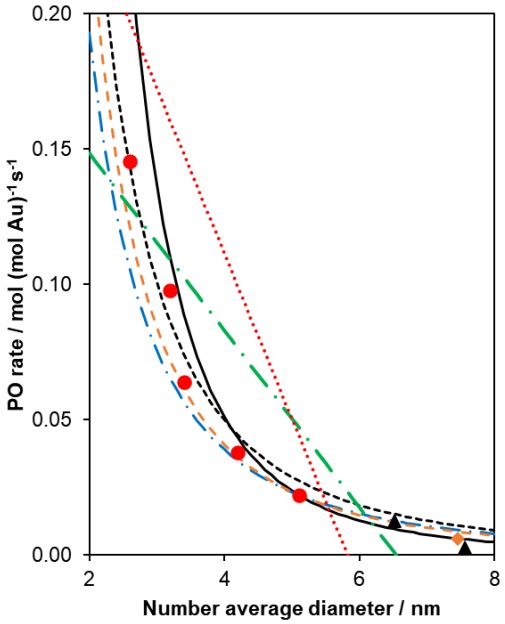

Figure 6: Model fits of experimental data for the data set consisting of 0.083Au-PVP/TS-1(126) catalysts (▲), 0.11Au-PVP/TS-1(73) (♦) and Au-DP/TS-1(100) catalysts (●) reported in [20], for the corner (black line), edge (blue dash-dot), perimeter (short orange dashes), proximal Ti (black dashes), terrace (green dash-dot), and surface (red dots) models. Reaction conditions: 10/10/10/70 mol% $C_3H_6/H_2/O_2/N_2$, SV = 14,000 $cm^3\ h^{-1}\ g_{cat}^{-1}$, T = 473 K, P = 101.3 kPa.

(equations shown in the SI, Section S.9). The corner, edge, and terrace atoms are mutually exclusive, however, the perimeter model includes a combination of corner, edge, and terrace atoms, and the surface model includes all accessible surface Au. These models assume that a single type of site (e.g., only 5- and 6-coordinate corner atoms closest to the support surface) makes up the vast majority of gold active sites. Further details of these models are shown in the Supporting Information (Sections S.9 and S.11). Additionally, a model of a non-faceted spherical nanoparticle was considered, as the TEM data considered here shows no clear evidence of faceted nanoparticles.[43] For the model regressions to propylene epoxidation rate data (Section S.11), in general the residual plots exhibited trends which resulted in clustering around y=x in the lag plots. This indicates the presence of systematic errors, meaning that the spherical nanoparticle model may not be a suitable fit for the data.

Since all the models mentioned so far only consider Au sites and do not consider Au-Ti interactions, we attempt to develop a new active site model here. Assuming a Langmuir-Hinshelwood-Hougen-Watson type mechanism, the reaction orders reported here, as well as all others reported previously are consistent with a reaction mechanism which requires the Au and Ti sites to be close enough to allow for interaction of Au- and Ti-bound reaction intermediates during the rate determining step.[19,20,36,44] An alternative mechanistic proposal requires the desorption and migration of hydrogen peroxide.[36] All reported reaction orders for the gas phase epoxidation of propylene with oxygen and hydrogen over Au/TS-1 catalysts typically have a hydrogen order near unity and an oxygen order of approximately 0.5, if one assumes a PO reaction order of -0.6, as this is the

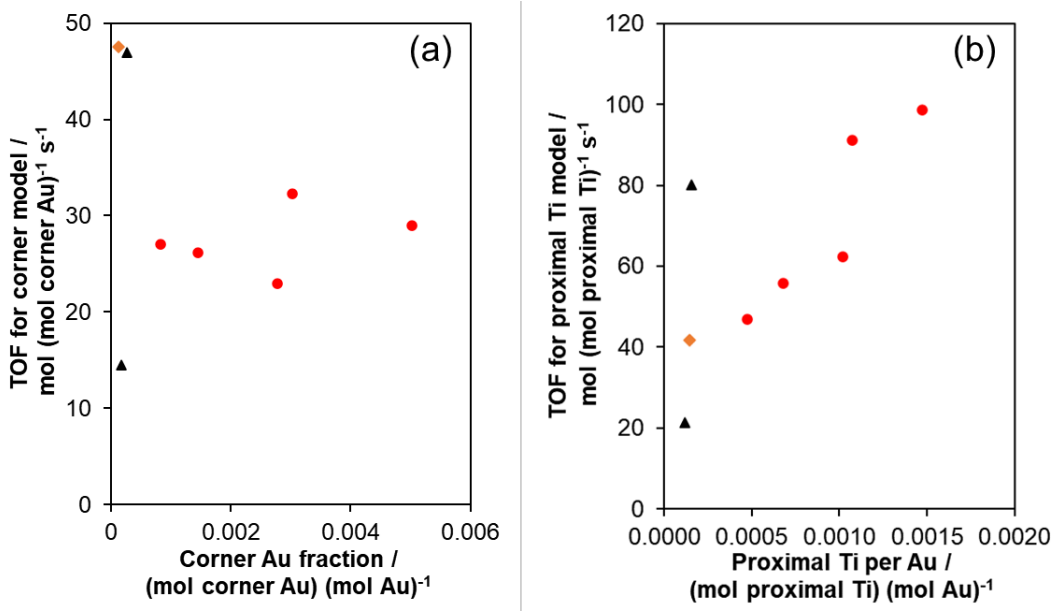

Figure 7: Plots of predicted TOF for the corner model (a) and proximal Ti model (b) as a function of the calculated site densities for Au-PVP/TS-1 (Si/Ti = 126) (▲), Au-PVP/TS-1 (Si/Ti = 73) (♦) and Au-DP/TS-1(100) catalysts ([40], ●). Reaction conditions: 10/10/10/70 mol% $C_3H_6/H_2/O_2/N_2$, SV = 14,000 $cm^3\ h^{-1}\ g_{cat}^{-1}$, T = 473 K, P = 101.3 kPa. For the proximal Ti model, a Au-Ti interaction range of 0.44 nm was used.

approximate value reported by all those who have measured the reaction order with respect to PO and corrected measured H_2 and O_2 reaction orders accordingly.[19,20,36,44] Therefore, given the hypothesis that Au-Ti proximity is necessary for PO-producing Au-Ti active sites, such proximity was used as a constraint for this active site model which we refer to as the 'proximal Ti' model in an attempt to test this hypothesis. This model predicts the number of Ti-containing sites on the external surfaces of TS-1 within a specified distance of the base of a gold nanoparticle which is itself on an external crystallite surface. We refer to the range in which Ti are considered proximal to a gold nanoparticle as the interaction range, and the bounds on this range are as follows: the distance from the center of the gold nanoparticle to the Ti site must be greater than the nanoparticle's radius, such that it is not covered by the nanoparticle, but less than the combined lengths of propylene and hydrogen peroxide (Figure S.16), which gives a maximum allowable distance of 0.44 nm before a gold nanoparticle and Ti site are no longer considered close enough to interact. This interaction range could be modified to increase physical accuracy in the future, but this was used as an initial guess to allow prediction of trends by the model. As a result of using the combined lengths of hydrogen peroxide and propylene for the maximum interaction range, turnover frequencies estimated using this assumption for the Au-Ti interaction range represent a minimum of the estimated catalytic turnover frequency required for the simultaneous mechanism alone to explain the observed rate of propylene epoxidation. Increasing this range decreases the predicted TOF, and decreasing this range increases the predicted TOF (Figure S.20). Using this model we can predict the approximate number of 'proximal Ti' per Au nanoparticle for a given Ti surface density, (here, the surface Si/Ti ratio was assumed to be equal to the bulk Si/Ti ratio), maximum interaction distance, and Au nanoparticle size. Further details of this model are shown in the Supporting Information (Section S.11) and a comparison of the regressions for all models considered here is shown in Figure 6.

For each model considered, the regression to the dataset consisting of rate vs. average diameter data for both Au-PVP/TS-1 and Au-DP/TS-1 catalysts was determined (Figure 6) by minimizing equation 7. For the catalyst samples in this study, the fraction of terrace and surface atoms scaled linearly with the average diameter and were therefore not considered. The corner, edge, perimeter, and 'proximal Ti' site densities were best approximated by power law relationships of $d^{-3.43}$, $d^{-2.31}$, $d^{-2.51}$, and $d^{-2.45}$, respectively. The rate of propylene epoxidation varies with the average diameter as $d^{-3.35}$. While the terrace and surface atom models can be disregarded due to their poor fits of the data, the corner, edge, perimeter, and proximal Ti models are difficult to distinguish and appear to all capture the trends in the data similarly (residual plots and lag plots in Section S.11). Since the 'proximal Ti' model is a modified perimeter model which accounts for Ti effects, and the edge model is essentially a perimeter model in which only a subset of perimeter Au atoms are considered (see Sections S.7, S.9), we chose to consider only the corner and proximal Ti models.

These active site models were used in conjunction with estimates of Ti densities on external crystallite surfaces and TEM measurements of the gold nanoparticle size distribution to calculate the catalytic turnover frequency required to explain the measured rate for each sample. Although there is the potential for Au clusters too small for detection by TEM on the ~200 nm TS-1 crystallites, the estimated turnover frequencies on Au-PVP/TS-1 catalysts, which have exclusively extracrystalline gold nanoparticles, span the range of predicted turnover frequencies for the Au-DP/TS-1 samples (Figure 7). Therefore, it is unlikely that a subset of Au clusters which is undetectable by TEM for Au-DP/TS-1 samples significantly influences the predicted values of TOF for each model considered here, and any contributions from such sites would reduce the calculated TOF values. The range of these predicted TOFs as a function of the fraction of corner Au sites or proximal sites are shown in Figure 7, and the relationship between the estimated active site density and the rate of propylene epoxidation normalized to gold content is shown

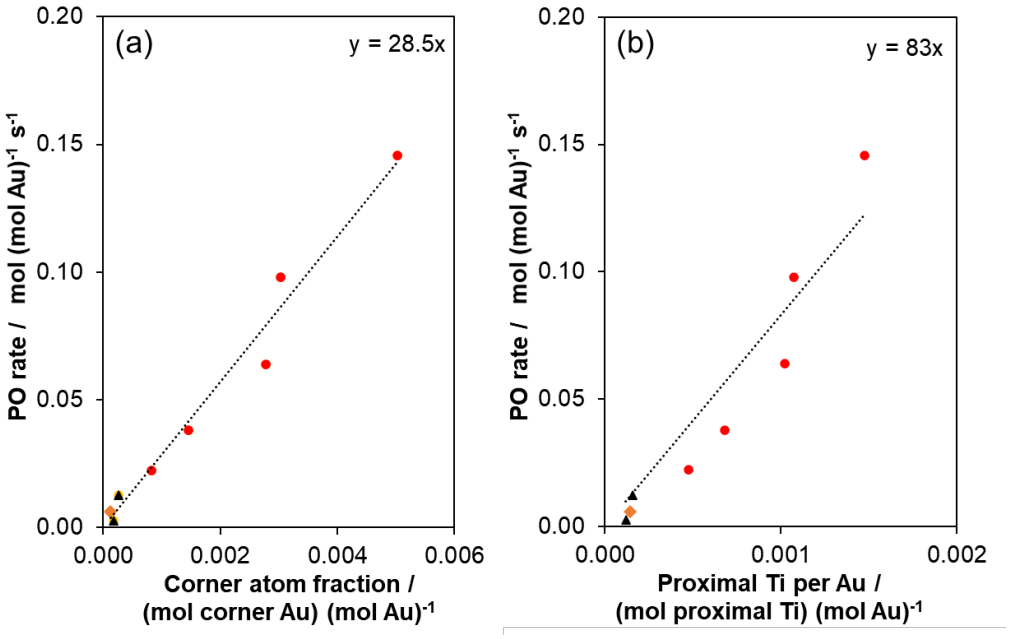

Figure 8: PO rate normalized to total gold mass vs. corner Au fraction (a) and proximal Ti per Au (b) for Au-PVP/TS-1 (Si/Ti = 126) (▲), Au-PVP/TS-1 (Si/Ti = 73) (♦), and Au-DP/TS-1 ([40], ●) catalysts. For the proximal Ti model, a Au-Ti interaction distance of 0.44 nm was used. The slope of the plotted line corresponds to the best-fit turnover frequency for the entire data set, which is shown in the upper righthand corner of each plot. Reaction conditions: 10/10/10/70 mol% $C_3H_6/H_2/O_2/N_2$, SV = 14,000 $cm^3\ h^{-1}\ g_{cat}^{-1}$, T = 473 K, P = 101.3 kPa.

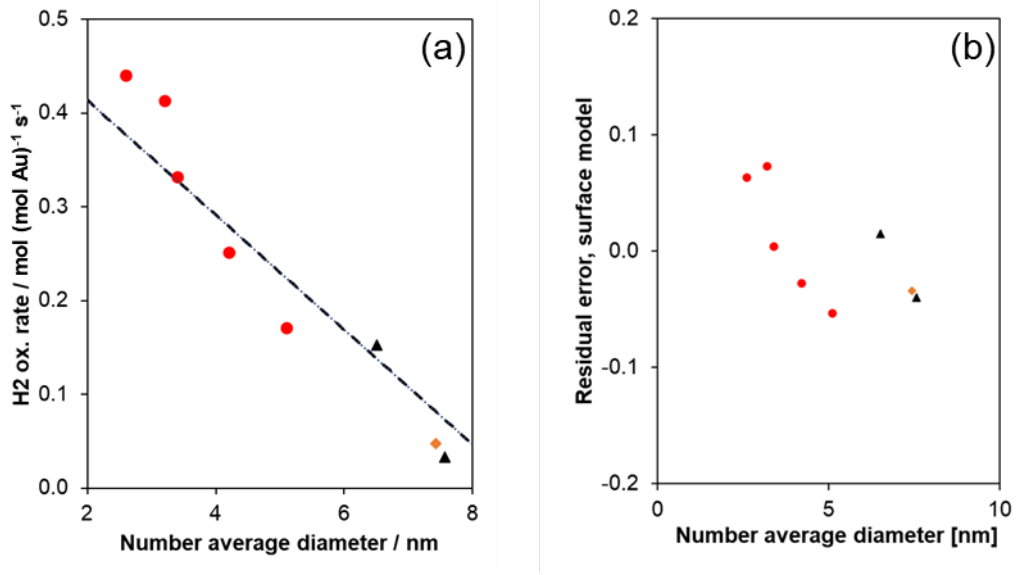

Figure 9: (a) Model fit of experimental data for the hydrogen oxidation rate data set consisting of 0.083Au-PVP/TS-1(126) catalysts (▲), 0.11Au-PVP/TS-1(73) (♦) and Au-DP/TS-1(100) catalysts (●) reported in [40] for the surface atom model (prediction shown by dashed line). (b) Residual plot for the model regression in (a). Reaction conditions: 10/10/10/70 mol% $C_3H_6/H_2/O_2/N_2$, SV = 14,000 $cm^3\ h^{-1}\ g_{cat}^{-1}$, T = 473 K, P = 101.3 kPa.

in Figure 8. For the reaction conditions used to measure catalytic rates of propylene epoxidation on Au/TS-1 catalysts (10/10/10/70 mol% $C_3H_6/H_2/O_2/N_2$, 473 K, SV = 14,000 $cm^3\ g_{cat}^{-1}\ h^{-1}$), the upper limit on the turnover frequency set by collision theory (assuming every collision of gas-phase propylene with an adsorption site results in product formation, regardless of whether the propylene must migrate to an active site or not) is approximately 140 s^{-1}. These limits were calculated using equation 7 (adapted from [45]) with the assumptions that propylene behaves as an ideal gas and that propylene may adsorb at any T-site on an exposed TS-1 surface.

$$\nu_{coll} = \rho_n \sqrt{\frac{RT}{2\pi M}} \qquad (9)$$

Both models predict turnover frequencies (~30 s^{-1} and ~80 s^{-1} for the corner and proximal Ti models, respectively) which are of a similar value to the collision theory estimated maximum rate, and these estimated turnover frequencies are also significantly higher than those reported previously for oxidation reactions on metal catalysts under similar reaction conditions, including estimates for propylene epoxidation on Au and Ag clusters (~0.4 s^{-1} and ~2.5 s^{-1}, respectively, 473 K), CO oxidation on Pt (0.002-0.05 s^{-1}, 473 K), and WGS on Pt

and Au (both ~0.2 s^{-1}, 473 K).[46–50] For the corner model, which was originally employed by Feng et al. assuming a sequential mechanism involving hydrogen peroxide migration, this suggests that corner atoms alone are not capable of explaining the observed rates of propylene epoxidation.[40] For the proximal Ti model, this implies that the simultaneous mechanism alone cannot explain the observed rates of propylene epoxidation, and that invoking short range migration of hydrogen peroxide over at least several nanometers is necessary to explain the observed rates with plausible calculated TOFs. Increasing the interaction range for Ti sites and Au nanoparticles in the proximal Ti model to ~10 nanometers decreases the calculated TOF to values consistent with previous reports (Figure S.20). This suggests that while the simultaneous mechanism cannot be conclusively invalidated here, hydrogen peroxide migration is necessary to explain the observed catalytic rates of propylene epoxidation on Au/TS-1 catalysts.

The active site models discussed for propylene epoxidation were then regressed to the measured catalytic rates of hydrogen oxidation. The active site model which 'best' fit the hydrogen oxidation data, as determined by examination of the residual plots (Section S.11), was the surface atom model, which assumes all surface Au atoms contribute to hydrogen oxidation (Figure 9). Magnitudes of hydrogen oxidation turnover frequencies normalized per surface Au atoms are on the order of 1 s^{-1}, consistent with previous reports of oxidation reactions on noble or transition metal catalysts.[46,47,49,50] The agreement of this model across both Au-DP/TS-1 and Au-PVP/TS-1 catalysts suggests that differences observed in the activation energy and oxygen reaction order between these two types of samples (Table 4) are not due to a difference in active site type. We speculate that these observations may instead be rationalized by a change in either surface coverage regime or rate-determining step, though further investigation into the origins of this discrepancy are beyond the scope of the present study. Additionally, the agreement of estimated turnover frequencies across these catalysts suggests that hydrogen oxidation on gold nanoparticles is a structure insensitive reaction that can potentially be used for estimation of accessible Au surface areas under these reaction conditions.

CONCLUSIONS

Au-PVP/TS-1 catalysts were synthesized by a repeated incipient wetness impregnation procedure and cleaned of organic PVP ligand residue by a series of in situ pretreatments. The reaction orders and activation energies for propylene epoxidation measured over Au-PVP/TS-1 catalysts were measured in a CSTR, free from temperature and concentration gradients, and were identical within experimental uncertainty to values previously reported for Au-DP/TS-1 catalysts. This agreement suggests that gold active sites on catalysts with some fraction of gold existing as small, intraporous clusters inside TS-1 (Au-DP/TS-1) and gold active sites on catalysts with exclusively larger, extracrystalline gold nanoparticles (Au-PVP/TS-1) are energetically similar (i.e., similar binding energies, reaction barriers, catalytic turnover frequencies). Additionally, this similarity demonstrates that propylene epoxidation on Au-PVP/TS-1 catalysts likely occurs through the same mechanism as on Au/TS-1 catalysts prepared by deposition-precipitation. Estimates of turnover frequencies for propylene epoxidation derived from model regressions considered herein suggest that models which assume a relatively constant number of active sites per gold nanoparticle (corner, proximal Ti models) are most capable of explaining measured catalytic propylene epoxidation rates on Au/TS-1 catalysts. The magnitude of the TOF predictions for the corner model suggest that corner atoms alone cannot produce hydrogen peroxide at a rate consistent with the observed rates of propylene epoxidation on the catalysts studied here. The estimated TOFs for propylene epoxidation via the simultaneous mechanism over active sites described by the proximal Ti model are much larger than those for previously reported metal-catalyzed oxidation reactions, and approach the collision theory limit of approximately 140 s^{-1}. This suggests that the simultaneous mechanism alone cannot explain the measured data, and that hydrogen peroxide migration from Au sites to Ti sites is necessary to explain the observed rates of propylene epoxidation on the catalysts considered here.

The kinetics of hydrogen oxidation on Au-PVP/TS-1 and Au-DP/TS-1 catalysts primarily differ in the measured values of activation energy (Au-PVP/TS-1: ~4 kJ mol^{-1}, Au-DP/TS-1: ~30 kJ mol^{-1}) and oxygen reaction order (Au-PVP/TS-1: 0, Au-DP/TS-1: 0.4). The measured activation energy for hydrogen oxidation on Au-PVP/TS-1 catalysts is similar to estimates of the activation energy for O_2-assisted hydrogen dissociation on gold surfaces. Rates of hydrogen oxidation on both Au-PVP/TS-1 and Au-DP/TS-1 were regressed to the same active site models as discussed for propylene epoxidation. The rate of hydrogen oxidation correlates best with a surface Au atom model, suggesting that all surface gold atoms participate in hydrogen oxidation. Additionally, the agreement of active site model for hydrogen oxidation across both Au-DP/TS-1 and Au-PVP/TS-1 catalysts implies that there is no change in active site between the two catalysts, and that the difference in activation energy and oxygen order must be the result of a change in surface coverage regime or rate-determining step. Magnitudes of hydrogen oxidation turnover frequencies normalized per surface Au atoms are on the order of 1 s^{-1}, consistent with previous reports of oxidation reactions on noble or transition metal catalysts. These findings suggest that Au particle sizes should be minimized, in order to maximize the fraction of Au sites which participate in propylene oxide formation in conjunction with Ti sites, but that all Au sites on these Au particles will also participate in deleterious hydrogen oxidation, placing an upper limit on the possible H_2 selectivities over Au-Ti catalysts for direct propylene epoxidation.

AUTHOR INFORMATION

Corresponding Author

James W. Harris – Department of Chemical and Biological Engineering, The University of Alabama, 3043 H. M. Comer. Hall, 245 7th Avenue, Tuscaloosa, AL 35487, USA.

Authors

Jeremy W. Arvay – Charles D. Davidson School of Chemical Engineering, Purdue University, 480 Stadium Mall Drive, West Lafayette, IN 47907, USA.

Wei Hong – Department of Chemistry, Purdue University, 560 Oval Drive, West Lafayette, IN 47907, USA.

Christina Li – Department of Chemistry, Purdue University, 560 Oval Drive, West Lafayette, IN 47907, USA.

W. Nicholas Delgass[†] – Charles D. Davidson School of Chemical Engineering, Purdue University, 480 Stadium Mall Drive, West Lafayette, IN 47907, USA.

Fabio H. Ribeiro – Charles D. Davidson School of Chemical Engineering, Purdue University, 480 Stadium Mall

Drive, West Lafayette, IN 47907, USA.

Notes

[†]Published posthumously.

The authors declare no competing financial interest.

ASSOCIATED CONTENT

The Supporting Information is available free of charge via the Internet at http://pubs.acs.org.

Reactor schematics; XRD patterns, nitrogen physisorption isotherms of TS-1 and S-1 supports; UV-Vis spectra of TS-1 supports; Mears criterion and Thiele modulus calculations; CO_2 generation with $H_2/O_2/N_2$ feeds; PO consumption during PO reaction order measurement on Au-PVP/S-1; active site models; gold nanoparticle size distributions for Au-PVP/TS-1 and Au-PVP/S-1 catalysts; time-on-stream profiles of PO rate, PO selectivity, and propylene conversion on 0.083Au-PVP/TS-1(126).

ACKNOWLEDGMENT

The authors acknowledge funding from the U.S. Department of Energy, Office of Basic Energy Sciences, Chemical Sciences, under Grant DE-FG02-03ER15408, as well as from the National Science Foundation, under Grant CHE-2045013.

The authors would like to dedicate this manuscript to the memory of Nick Delgass, who sadly passed way during its completion. Nick was always tireless in both his pursuit of scientific truth and his support of students and younger colleagues. He will be dearly missed.

REFERENCES

(1) Baer, H.; Bergamo, M.; Forlin, A.; Pottenger, L. H.; Lindner, J. Propylene Oxide. In *Ullmann's Encyclopedia of Industrial Chemistry*; John Wiley & Sons, Ltd, 2012. https://doi.org/10.1002/14356007.a22_239.pub3.

(2) Nijhuis, T. A.; Makkee, M.; Moulijn, J. A.; Weckhuysen, B. M. The Production of Propene Oxide: Catalytic Processes and Recent Developments. *Ind. Eng. Chem. Res.* **2006**, *45* (10), 3447–3459. https://doi.org/10.1021/ie0513090.

(3) Lu, J.; Zhang, X.; Bravo-Suárez, J. J.; Fujitani, T.; Oyama, S. T. Effect of Composition and Promoters in Au/TS-1 Catalysts for Direct Propylene Epoxidation Using H2 and O2. *Catal. Today* **2009**, *147* (3–4), 186–195. https://doi.org/10.1016/j.cattod.2008.09.005.

(4) Haruta, M.; Uphade, B. S.; Tsubota, S.; Miyamoto, A. Selective Oxidation of Propylene over Gold Deposited on Titanium-Based Oxides. *Res. Chem. Intermed.* **1998**, *24* (3), 329–336. https://doi.org/10.1163/156856798X00276.

(5) Bravo-Suárez, J. J.; Lu; Dallos, C. G.; Fujitani, T.; Oyama, S. T. Kinetic Study of Propylene Epoxidation with H2 and O2 over a Gold/Mesoporous Titanosilicate Catalyst. *J. Phys. Chem. C* **2007**, *111* (46), 17427–17436. https://doi.org/10.1021/jp075098j.

(6) Sinha, A. K.; Seelan, S.; Okumura, M.; Akita, T.; Tsubota, S.; Haruta, M. Three-Dimensional Mesoporous Titanosilicates Prepared by Modified Sol−Gel Method: Ideal Gold Catalyst Supports for Enhanced Propene Epoxidation. *J. Phys. Chem. B* **2005**, *109* (9), 3956–3965. https://doi.org/10.1021/jp0465229.

(7) Uphade, B. S.; Akita, T.; Nakamura, T.; Haruta, M. Vapor-Phase Epoxidation of Propene Using H2 and O2 over Au/Ti–MCM-48. *J. Catal.* **2002**, *209* (2), 331–340. https://doi.org/10.1006/jcat.2002.3642.

(8) Uphade, B. S.; Yamada, Y.; Akita, T.; Nakamura, T.; Haruta, M. Synthesis and Characterization of Ti-MCM-41 and Vapor-Phase Epoxidation of Propylene Using H2 and O2 over Au/Ti-MCM-41. *Appl. Catal. Gen.* **2001**, *215* (1), 137–148. https://doi.org/10.1016/S0926-860X(01)00527-0.

(9) Lu, J.; Zhang, X.; Bravo-Suárez, J. J.; Bando, K. K.; Fujitani, T.; Oyama, S. T. Direct Propylene Epoxidation over Barium-Promoted Au/Ti-TUD Catalysts with H2 and O2: Effect of Au Particle Size. *J. Catal.* **2007**, *250* (2), 350–359. https://doi.org/10.1016/j.jcat.2007.06.006.

(10) Hayashi, T.; Tanaka, K.; Haruta, M. Selective Vapor-Phase Epoxidation of Propylene over Au/TiO2Catalysts in the Presence of Oxygen and Hydrogen. *J. Catal.* **1998**, *178* (2), 566–575. https://doi.org/10.1006/jcat.1998.2157.

(11) Qi, C.; Huang, J.; Bao, S.; Su, H.; Akita, T.; Haruta, M. Switching of Reactions between Hydrogenation and Epoxidation of Propene over Au/Ti-Based Oxides in the Presence of H2 and O2. *J. Catal.* **2011**, *281* (1), 12–20. https://doi.org/10.1016/j.jcat.2011.03.028.

(12) Huang, J.; Takei, T.; Akita, T.; Ohashi, H.; Haruta, M. Gold Clusters Supported on Alkaline Treated TS-1 for Highly Efficient Propene Epoxidation with O2 and H2. *Appl. Catal. B Environ.* **2010**, *95* (3–4), 430–438. https://doi.org/10.1016/j.apcatb.2010.01.023.

(13) Lee, W.-S.; Cem Akatay, M.; Stach, E. A.; Ribeiro, F. H.; Nicholas Delgass, W. Enhanced Reaction Rate for Gas-Phase Epoxidation of Propylene Using H2 and O2 by Cs Promotion of Au/TS-1. *J. Catal.* **2013**, *308*, 98–113. https://doi.org/10.1016/j.jcat.2013.05.023.

(14) Barrio, L.; Liu, P.; Rodriguez, J. A.; Campos-Martin, J. M.; Fierro, J. L. G. Effects of Hydrogen on the Reactivity of O2 toward Gold Nanoparticles and Surfaces. *J. Phys. Chem. C* **2007**, *111* (51), 19001–19008. https://doi.org/10.1021/jp073552d.

(15) Lang, S. M.; Bernhardt, T. M.; Barnett, R. N.; Yoon, B.; Landman, U. Hydrogen-Promoted Oxygen Activation by Free Gold Cluster Cations. *J. Am. Chem. Soc.* **2009**, *131* (25), 8939–8951. https://doi.org/10.1021/ja9022368.

(16) Barton, D. G.; Podkolzin, S. G. Kinetic Study of a Direct Water Synthesis over Silica-Supported Gold

Nanoparticles. *J. Phys. Chem. B* **2005**, *109* (6), 2262–2274. https://doi.org/10.1021/jp048837u.

(17) Lee, W.-S.; Cem Akatay, M.; Stach, E. A.; Ribeiro, F. H.; Nicholas Delgass, W. Reproducible Preparation of Au/TS-1 with High Reaction Rate for Gas Phase Epoxidation of Propylene. *J. Catal.* **2012**, *287*, 178–189. https://doi.org/10.1016/j.jcat.2011.12.019.

(18) Lee, W.-S.; Lai, L.-C.; Cem Akatay, M.; Stach, E. A.; Ribeiro, F. H.; Delgass, W. N. Probing the Gold Active Sites in Au/TS-1 for Gas-Phase Epoxidation of Propylene in the Presence of Hydrogen and Oxygen. *J. Catal.* **2012**, *296*, 31–42. https://doi.org/10.1016/j.jcat.2012.08.021.

(19) Taylor, B.; Lauterbach, J.; Blau, G. E.; Delgass, W. N. Reaction Kinetic Analysis of the Gas-Phase Epoxidation of Propylene over Au/TS-1. *J. Catal.* **2006**, *242* (1), 142–152. https://doi.org/10.1016/j.jcat.2006.06.007.

(20) Harris, J. W.; Arvay, J.; Mitchell, G.; Delgass, W. N.; Ribeiro, F. H. Propylene Oxide Inhibits Propylene Epoxidation over Au/TS-1. *J. Catal.* **2018**, *365*, 105–114. https://doi.org/10.1016/j.jcat.2018.06.015.

(21) Bukowski, B. C.; Delgass, W. N.; Greeley, J. Gold Stability and Diffusion in the Au/TS-1 Catalyst. *J. Phys. Chem. C* **2021**, *125* (8), 4519–4531. https://doi.org/10.1021/acs.jpcc.0c10193.

(22) Otto, T.; Zhou, X.; Zones, S. I.; Iglesia, E. Synthesis, Characterization, and Function of Au Nanoparticles within TS-1 Zeotypes as Catalysts for Alkene Epoxidation Using O2/H2O Reactants. *J. Catal.* **2022**, *410*, 206–220. https://doi.org/10.1016/j.jcat.2022.04.002.

(23) Khomane, R. B.; Kulkarni, B. D.; Paraskar, A.; Sainkar, S. R. Synthesis, Characterization and Catalytic Performance of Titanium Silicalite-1 Prepared in Micellar Media. *Mater. Chem. Phys.* **2002**, *76* (1), 99–103. https://doi.org/10.1016/S0254-0584(01)00507-7.

(24) Tsunoyama, H.; Sakurai, H.; Negishi, Y.; Tsukuda, T. Size-Specific Catalytic Activity of Polymer-Stabilized Gold Nanoclusters for Aerobic Alcohol Oxidation in Water. *J. Am. Chem. Soc.* **2005**, *127* (26), 9374–9375. https://doi.org/10.1021/ja052161e.

(25) Tsunoyama, H.; Sakurai, H.; Ichikuni, N.; Negishi, Y.; Tsukuda, T. Colloidal Gold Nanoparticles as Catalyst for Carbon−Carbon Bond Formation: Application to Aerobic Homocoupling of Phenylboronic Acid in Water. *Langmuir* **2004**, *20* (26), 11293–11296. https://doi.org/10.1021/la0478189.

(26) Tauc, J. Optical Properties and Electronic Structure of Amorphous Ge and Si. *Mater. Res. Bull.* **1968**, *3* (1), 37–46. https://doi.org/10.1016/0025-5408(68)90023-8.

(27) Tauc, J.; Grigorovici, R.; Vancu, A. Optical Properties and Electronic Structure of Amorphous Germanium. *Phys. Status Solidi B* **1966**, *15* (2), 627–637. https://doi.org/10.1002/pssb.19660150224.

(28) Davis, E. A.; Mott, N. F. Conduction in Non-Crystalline Systems V. Conductivity, Optical Absorption and Photoconductivity in Amorphous Semiconductors. *Philos. Mag. J. Theor. Exp. Appl. Phys.* **1970**, *22* (179), 0903–0922. https://doi.org/10.1080/14786437008221061.

(29) Jiao, Y.; Adedigba, A.-L.; Dummer, N. F.; Liu, J.; Zhou, Y.; Guan, Y.; Shen, H.; Perdjon, M.; Hutchings, G. J. The Effect of T-Atom Ratio and TPAOH Concentration on the Pore Structure and Titanium Position in MFI-Type Titanosilicate during Dissolution-Recrystallization Process. *Microporous Mesoporous Mater.* **2020**, *305*, 110397. https://doi.org/10.1016/j.micromeso.2020.110397.

(30) Feng, X.; Song, Z.; Liu, Y.; Chen, X.; Jin, X.; Yan, W.; Yang, C.; Luo, J.; Zhou, X.; Chen, D. Manipulating Gold Spatial Location on Titanium Silicalite-1 To Enhance the Catalytic Performance for Direct Propene Epoxidation with H2 and O2. *ACS Catal.* **2018**, *8* (11), 10649–10657. https://doi.org/10.1021/acscatal.8b02836.

(31) Gounder, R.; Davis, M. E. Titanium-Beta Zeolites Catalyze the Stereospecific Isomerization of D-Glucose to L-Sorbose via Intramolecular C5–C1 Hydride Shift. *ACS Catal.* **2013**, *3* (7), 1469–1476. https://doi.org/10.1021/cs400273c.

(32) Xue, X.; Ji, W.; Mao, Z.; Mao, H.; Wang, Y.; Wang, X.; Ruan, W.; Zhao, B.; Lombardi, J. R. Raman Investigation of Nanosized TiO2: Effect of Crystallite Size and Quantum Confinement. *J. Phys. Chem. C* **2012**, *116* (15), 8792–8797. https://doi.org/10.1021/jp2122196.

(33) Behrens, M.; Schlögl, R. X-Ray Diffraction and Small Angle X-Ray Scattering. In *Characterization of Solid Materials and Heterogeneous Catalysts*; John Wiley & Sons, Ltd, 2012; pp 609–653. https://doi.org/10.1002/9783527645329.ch15.

(34) Zhang, H.; Banfield, J. F. Understanding Polymorphic Phase Transformation Behavior during Growth of Nanocrystalline Aggregates: Insights from TiO2. *J. Phys. Chem. B* **2000**, *104* (15), 3481–3487. https://doi.org/10.1021/jp000499j.

(35) Wang, Z.; Liu, X.; Lv, M.; Chai, P.; Liu, Y.; Meng, J. Preparation of Ferrite MFe2O4 (M = Co, Ni) Ribbons with Nanoporous Structure and Their Magnetic Properties. *J. Phys. Chem. B* **2008**, *112* (36), 11292–11297. https://doi.org/10.1021/jp804178w.

(36) Lu, J.; Zhang, X.; Bravo-Suárez, J. J.; Tsubota, S.; Gaudet, J.; Oyama, S. T. Kinetics of Propylene Epoxidation Using H2 and O2 over a Gold/Mesoporous Titanosilicate Catalyst. *Catal. Today* **2007**, *123* (1–4), 189–197. https://doi.org/10.1016/j.cattod.2007.02.005.

(37) Tsilingiris, P. T. Thermophysical and Transport Properties of Humid Air at Temperature Range between 0 and 100°C. *Energy Convers. Manag.* **2008**, *49* (5), 1098–1110. https://doi.org/10.1016/j.enconman.2007.09.015.

(38) Kul'kova, N. V.; Levchenko, L. P. *Kinet Katal* **1965**, *6*, 765.

(39) Choi, K.-H.; Coh, B.-Y.; Lee, H.-I. Properties of Adsorbed Oxygen on Au/SiO2. *Catal. Today* **1998**, *44* (1), 205–213. https://doi.org/10.1016/S0920-5861(98)00192-8.

(40) Feng, X.; Duan, X.; Qian, G.; Zhou, X.; Chen, D.; Yuan, W. Insights into Size-Dependent Activity and Active Sites of Au Nanoparticles Supported on TS-1 for Propene Epoxidation with H2 and O2. *J. Catal.* **2014**, *317*, 99–104. https://doi.org/10.1016/j.jcat.2014.05.006.

(41) Williams, W. D.; Shekhar, M.; Lee, W.-S.; Kispersky, V.; Delgass, W. N.; Ribeiro, F. H.; Kim, S. M.; Stach, E. A.; Miller, J. T.; Allard, L. F. Metallic Corner Atoms in Gold Clusters Supported on Rutile Are the Dominant Active Site during Water−Gas Shift Catalysis. *J. Am. Chem. Soc.* **2010**, *132* (40), 14018–14020. https://doi.org/10.1021/ja1064262.

(42) Van Hardeveld, R.; Hartog, F. The Statistics of Surface Atoms and Surface Sites on Metal Crystals. *Surf. Sci.* **1969**, *15* (2), 189–230. https://doi.org/10.1016/0039-6028(69)90148-4.

(43) Reske, R.; Mistry, H.; Behafarid, F.; Roldan Cuenya, B.; Strasser, P. Particle Size Effects in the Catalytic Electroreduction of CO2 on Cu Nanoparticles. *J. Am. Chem. Soc.* **2014**, *136* (19), 6978–6986. https://doi.org/10.1021/ja500328k.

(44) Oyama, S. T.; Zhang, X.; Lu, J.; Gu, Y.; Fujitani, T. Epoxidation of Propylene with H2 and O2 in the Explosive Regime in a Packed-Bed Catalytic Membrane Reactor. *J. Catal.* **2008**, *257* (1), 1–4. https://doi.org/10.1016/j.jcat.2008.04.023.

(45) Djéga-Mariadassou, G.; Boudart, M. *Kinetics of Heterogeneous Catalytic Reactions*; Princeton University Press, **1984**; pp 13.

(46) Lei, Y.; Mehmood, F.; Lee, S.; Greeley, J.; Lee, B.; Seifert, S.; Winans, R. E.; Elam, J. W.; Meyer, R. J.; Redfern, P. C.; Teschner, D.; Schlögl, R.; Pellin, M. J.; Curtiss, L. A.; Vajda, S. Increased Silver Activity for Direct Propylene Epoxidation via Subnanometer Size Effects. *Science* **2010**, 224–228.

(47) Lee, S.; Molina, L. M.; López, M. J.; Alonso, J. A.; Hammer, B.; Lee, B.; Seifert, S.; Winans, R. E.; Elam, J. W.; Pellin, M. J.; Vajda, S. Selective Propene Epoxidation on Immobilized Au6–10 Clusters: The Effect of Hydrogen and Water on Activity and Selectivity. *Angew. Chem. Int. Ed.* **2009**, *48* (8), 1467–1471. https://doi.org/https://doi.org/10.1002/anie.200804154.

(48) Moses-DeBusk, M.; Yoon, M.; Allard, L. F.; Mullins, D. R.; Wu, Z.; Yang, X.; Veith, G.; Stocks, G. M.; Narula, C. K. CO Oxidation on Supported Single Pt Atoms: Experimental and Ab Initio Density Functional Studies of CO Interaction with Pt Atom on θ-Al2O3(010) Surface. *J. Am. Chem. Soc.* **2013**, *135* (34), 12634–12645. https://doi.org/10.1021/ja401847c.

(49) Yang, M.; Li, S.; Wang, Y.; Herron, J. A.; Xu, Y.; Allard, L. F.; Lee, S.; Huang, J.; Mavrikakis, M.; Flytzani-Stephanopoulos, M. Catalytically Active Au-O(OH)x- Species Stabilized by Alkali Ions on Zeolites and Mesoporous Oxides. *Science* **2014**, *346* (6216), 1498–1501. https://doi.org/10.1126/science.1260526.

(50) Yang, M.; Liu, J.; Lee, S.; Zugic, B.; Huang, J.; Allard, L. F.; Flytzani-Stephanopoulos, M. A Common Single-Site Pt(II)–O(OH)x– Species Stabilized by Sodium on "Active" and "Inert" Supports Catalyzes the Water-Gas Shift Reaction. *J. Am. Chem. Soc.* **2015**, *137* (10), 3470–3473. https://doi.org/10.1021/ja513292k.

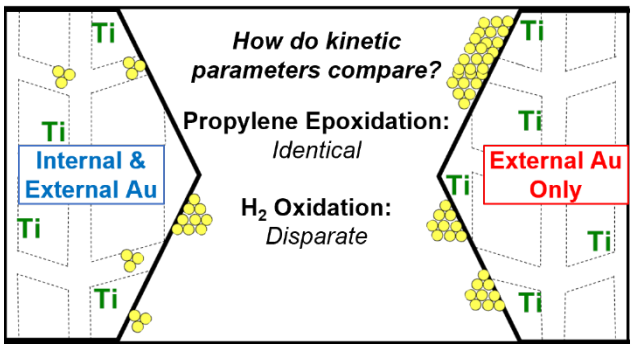

GRAPHICAL ABSTRACT